Biodegradable Theranostic Plasmonic Vesicles of Amphiphilic Gold Nanorods

Jibin Song, Lu Pu, Jiajing Zhou, Bo Duan, and Hongwei Duan*

School of Chemical and Biomedical Engineering, Nanyang Technological University, 70 Nanyang Drive, Singapore 637457

ABSTRACT We have developed surface-initiated organocatalytic ring-opening polymerization on functional nanocrystals and synthesized amphiphilic gold nanorods carrying well-defined mixed polymer brushes of poly(ethylene glycol) and polylactide. Self-assembly of the amphiphilic gold nanorods affords biodegradable plasmonic vesicles that can be destructed by both enzymatic degradation and near-infrared photothermal heating. When tagged with Raman probes, strongly coupled gold nanorods in the self-assembled vesicles give rise to highly active SERS signals. The biodegradable plasmonic vesicles exhibit a unique combination of optical and structural properties that are of particular interest for theranostic applications. We have demonstrated that bioconjugated SERS-active plasmonic vesicles can specifically target EpCAM-positive cancer cells, leading to ultrasensitive spectroscopic detection of cancer cells. Furthermore, integration of photothermal effect of gold nanorods and large loading capacity of the vesicles provides opportunities for localized synergistic photothermal ablation and photoactivated chemotherapy, which have shown higher efficiency in killing targeted cancer cells than either single therapeutic modality. The versatile chemistry of organocatalytic ring-opening polymerization, in conjugation with recent development in synthesizing functional nanocrystals with tailored optical, electronic, and magnetic properties opens the possibilities for constructing multifunctional biodegradable platforms for clinical translation.

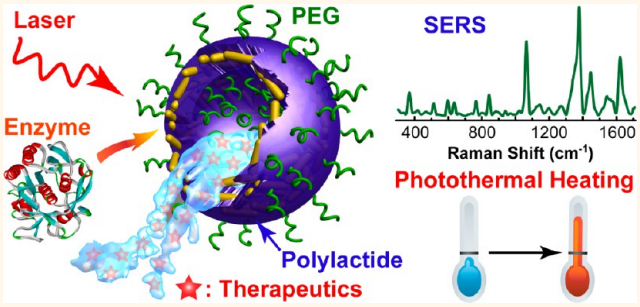

KEYWORDS: plasmonic vesicle · amphiphilic nanocrystal · surface-initiated organocatalytic ring-opening polymerization · chemo-photothermal therapy · SERS · theranostic nanomedicine

In this article, we present the development of biodegradable plasmonic vesicles, assembled from amphiphilic gold nanorods (AuNRs) carrying mixed polymer brushes of poly(ethylene glycol) (PEG) and polylactide (PLA), for simultaneous spectroscopic detection of cancer cells by surface enhanced Raman scattering (SERS) and combined chemo-photothermal therapy. Localized surface plasmon resonance (LSPR), leading to confined electromagnetic field surrounding plasmonic metal nanostructures, endows them with spectrally tunable optical and photothermal conversion properties that are of considerable interest for optoelectronics, biosensing, and nanomedicine.[1,2] LSPR of plasmonic nanostructures can be broadly tailored by modulating their intrinsic structural parameters and immediate environment such as dielectric property of local medium and separating distance of neighboring nanoparticles.[3] Consequently, while intense research has focused on wet-chemical synthesis of plasmonic metal nanostructures with controlled size, morphology, and chemical configuration,[4−6] parallel efforts have also been made to organize them into assemblies with collective properties significantly different from that of their building blocks.[7−10] The signal contrast between the assemblies and their building blocks, governed by interparticle-spacing dependent plasmonic coupling, has found widespread uses in plasmonic nanosensors and surface enhanced spectroscopy.[11,12] For example, the interstitial spaces and nanoparticle junctions in strongly coupled plasmonic assemblies can serve as SERS hotspots, leading to dramatically amplified Raman signals for sensitive detection of biological and small molecular targets.[13,14]

Self-assembly of plasmonic nanostructures into well-defined discrete ensembles rather than irregular macroscopic aggregates has received increasing attention because of fundamental interest in plasmon hybridization in molecular-like structures and applications in living systems with size-limited biological barriers.[15−17] Surface coatings,

* Address correspondence to hduan@ntu.edu.sg.

Received for review July 24, 2013 and accepted September 29, 2013.

Published online September 30, 2013
10.1021/nn403846v

primarily biomolecules and synthetic polymers, play major roles in directing the self-assembly of functional nanocrystals by imparting specific recognition and association mechanisms to the hybrid nanoparticles.[18,19] Recent research by several groups including us has developed a new class of plasmonic building blocks based on amphiphilic polymer brush coatings, which allow for amphiphilicity-driven self-assembly of plasmonic nanostructures in aqueous medium, leading to well-defined ensembles ranging from multimers to tubules and vesicles.[20−26] Amphiphilic polymer brushes were generally attached on nanostructures in a "grafting to" manner through ligand exchange reactions with end-functionalized polymers. Our recent results have demonstrated that tandem "grafting to" and "grafting from" (surface-initiated polymerization) of amphiphilic mixed brushes allows for efficient loading of the brushes with precisely controlled structures (molecular weight, graft density, relative ratio, and pedant functionality) on high-quality plasmonic nanostructures of selective sizes and morphologies.[27] Additionally, in comparison with the common method solely based on "grafting to", which results in low graft density due to interchain steric hindrance, this two-step strategy provides opportunities for grafting a diverse range of functional polymers on the plasmonic "core" nanoparticles in high graft densities. On the other hand, it is noteworthy that polymerization techniques currently applicable for grafting from plasmonic nanostructures, *i.e.*, controlled free radical polymerization only allows for controlled growth of polymer grafts with nondegradable hydrocarbon main chains.[28] However, the increasing biomedical uses of plasmonic nanomaterials have created growing demands for polymeric coatings with well-established biodegradability and biocompatibility.[29]

In the current study, we achieved sequentially conducted ligand exchange and surface initiated organocatalytic living ring-opening polymerization (ROP) for synthesizing amphiphilic AuNRs coated with mixed PEG and PLA brushes (AuNR@PEG/PLA), and further assembled them into biodegradable plasmonic vesicles for theranostic applications. Our work represents the first example of surface-initiated living ROP of biodegradable polymers on plasmonic nanoparticles. A major challenge for surface initiated polymerization on functional nanocrystals is to maintain the stable binding of surface-immobilized initiators and colloidal stability of the nanocrystals. For metal nanostructures, initiators are typically anchored by forming metal−sulfur bonds, which become labile at high temperature conditions (>60 °C).[30,31] Organocatalytic ROP has emerged as a versatile polymerization technique for biodegradable polyesters and polycarbonates.[32] Of particular importance is that appropriate combination of organic catalysts and solvent systems allows for low-temperature (<40 °C) living polymerization of a broad spectrum of cyclic monomers including lactide (LA), in contrast to metal-catalyzed ROP requiring high temperature (>100 °C),[33] making it possible for the living growth of biodegradable polymers on plasmonic nanostructures.

Multifunctional theranostic platforms hold great promise in nanomedicine by coupling diagnostic and therapeutic modalities for simultaneous imaging/detection and treatment, which are essential for traceable drug delivery and imaging-guided therapy.[34−38] Here, self-assembly of amphiphilic AuNR@PEG/PLA nanoparticles leads to well-defined vesicles consisting of AuNRs embedded PLA shell and PEG corona at both sides of the hydrophobic shell, as illustrated in Figure 1. The AuNR@PEG/PLA plasmonic vesicles exhibit a unique combination of optical and structural properties that are of particular interest for theranostic applications. First, all of the three components of the AuNR@PEG/PLA naoparticles have excellent biocompatibility proven in medical applications. PEG with excellent protein resistant property is among the most widely used polymers in biotechnology and pharmaceuticals.[39] PLA and its copolymers have been widely explored for biodegradable biomedical devices, tissue engineering scaffolds, and controlled drug release.[40] Polymeric micelles of PEG-*b*-PLA block copolymers encapsulating anticancer drug paclitaxel have been approved by the Food and Drug Administration for the treatment of advanced breast cancer.[41] And pegylated gold nanostructures are under active development in a variety of preclinical studies.[42−44] Second, when tagged with Raman probes, strongly coupled AuNRs in the self-assembled vesicles give rise to highly active SERS signals, which enable the ultrasensitive spectroscopic detection of targeted cancer cells labeled with bioconjugated plasmonic vesicles. Recent advances in developing SERS-encoded plasmonic nanostructures that generate stable and reproducible signals have made Raman imaging and spectroscopy an intriguing diagnostic tool for clinical uses.[45−47] Importantly, the aspect ratio-dependent longitudinal LSPR of AuNRs,[48,49] in conjugation with the controlled plasmonic coupling in the vesicles, allows for tuning the LSPR of plasmonic vesicles into near-infrared (NIR) spectral window, which is essential for clinical translation of AuNRs@PEG/PLA vesicles because of better tissue penetration depth. Third, the plasmonic vesicle offers both hydrophobic PLA shell and large aqueous cavity for loading of anticancer therapeutics of diverse physiochemical properties. Integration of the highly efficient photothermal effect of AuNRs and large loading capacity of the vesicles provides opportunities for localized synergistic photothermal ablation and photoactivated chemotherapy, which have shown higher efficiency in killing targeted cancer cells than either single therapeutic modality because cells under hyperthermia become more vulnerable to chemotherapy.[50,51]

RESULTS AND DISCUSSION

Synthesis and Self-Assembly of Amphiphilic AuNR@PEG/PLA. SERS-active amphiphilic AuNRs were synthesized in a two-step reaction starting with anchoring hydrophilic

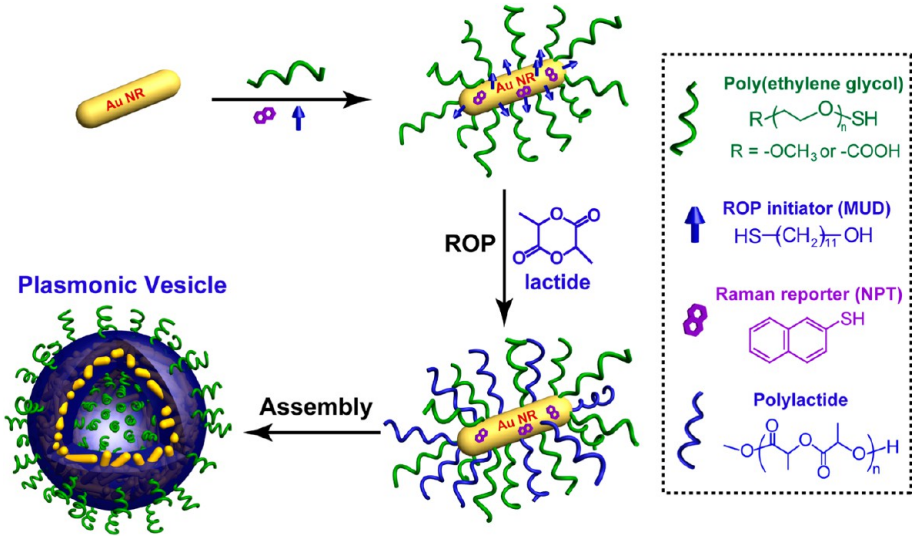

Figure 1. Schematic illustration of the synthesis of SERS-active amphiphilic gold nanorods with mixed polymer brushes PEG and PLA (AuNR@PEG/PLA) in the sequentially combined "grafting to" (coadsorption PEG, Raman reporter and ROP initiator) and "grafting from" (organocatalytic surface-initiated ROP) approaches and self-assembly of AuNR@PEG/PLA into plasmonic vesicles.

PEG (M_n = 5 kDa), initiator of organocatalytic ROP, and Raman probe on AuNRs by ligand exchange, followed by 4-dimethylaminopyridine (DMAP) catalyzed surface-initiated ROP of lactide (Figure 1). To facilitate the binding of hydrophobic ROP initiator, *i.e.*, 11-mercapto-1-undecanol (MUD) and Raman probe, *i.e.*, 2-naphthalenethiol (NPT) on hydrophilic AuNRs stabilized by cetyltrimethylammonium bromide (CTAB), the AuNRs dispersed in water were first pretreated with a weak ligand, *i.e.*, 2-(2-aminoethoxy)ethanol to transfer the nanorods into dimethyl sulfoxide (DMSO). Afterward, ligand exchange followed with a mixture of PEG (40 mg), MUD (6.5 mg), and NPT (0.12 mg) with a molar ratio of 5:20:1 in DMSO for 12 h, and the surface-functionalized AuNRs were purified by repeated centrifugation and redispersion. ^{1}H NMR spectrum (Figure S1) of mixed PEG and MUD ligands detached from AuNRs shows that the actual PEG/MUD ratio on AuNRs is 1:23, which is reasonable because small molecular MUD can be anchored on AuNR surfaces more efficiently than PEG. The resultant AuNRs (AuNR@PEG/MUD) were well-dispersed in polar solvents like DMSO, but not in nonpolar solvents such as chloroform (inset in Figure 2a). The formation of insoluble aggregates is possibly due to the polar hydroxyl end group of MUD and hydrogen bonding between the hydroxyl groups in MUD and oxygen atoms in PEG. Since the organocatalytic ROP necessitates nonpolar solvents such as chloroform and toluene, the AuNRs were suspended in chloroform and used as macroinitiator for DMAP-catalyzed ROP of lactide. Surprisingly, after the polymerization progressed for 1 h at 40 °C, the insoluble AuNR precipitates completely dissolved and formed a homogeneous dispersion (inset in Figure 2a and Movie in Supporting Information). Apparently, the growth of the PLA grafts on the AuNRs improved their solubility in chloroform. UV−vis spectra (Figure 2a) show that the longitudinal LSPR of AuNRs (~13 nm × 46 nm) (Figure S2) with an aspect ratio of 3.5 red-shifted from 745 to 778 nm in AuNR@PEG/PLA because of increased refractive index of the polymer coating.

Gel permeation chromatography (GPC) measurements (Figure 2b) show that the PLA brushes have low polydispersity (1.08−1.14) and their molecular weights increase from 6.5 to 13 and 21 kDa at reaction time of 8, 13, and 20 h, respectively, thanks to the living ROP of lactide catalyzed by DMAP.[52] The characteristic resonances of PEG at 3.65 ppm (−CH_2−CH_2−O) and PLA at 1.54 (CH_3−) and 5.18 ppm (−CH(CH_3)−) were detected in ^{1}H NMR spectra (Figure 2c) of AuNR@PEG/PLA, and stronger PLA signals were found for the samples with longer PLA grafts. Similarly, the growth of PLA grafts in AuNR@PEG/PLA from 6.5 to 13 and 21 kDa led to a gradual increase of polymer weight fraction from 8.7% to 13.5% and 19.3% (Figure 2d) in thermogravimetric analysis (TGA). A PEG/PLA molar ratio of 1:2.5 is calculated from the results of GPC and ^{1}H NMR analysis, which, in combination with the weight fraction determined by TGA, give rise to a polymer graft density of ~0.5 chain/nm^2 (see Supporting Information). An initiator efficiency of 11% in the surface-initiated organocatalytic ROP can be deduced from the PEG/PLA (1:2.5) and PEG/MUD (1: 23) ratios collectively (see Supporting Information). The graft density achieved is similar to what we obtained in surface initiated atom transfer radical polymerization (ATRP),[27] corresponding to an average number of 1090 polymer grafts (310 PEG chains and 780 PLA chains) per nanorod. In contrast, the one-step "grafting to" modification using thiolated PEG (M_n = 5 kDa) and PLA (M_n = 21 kDa) of the

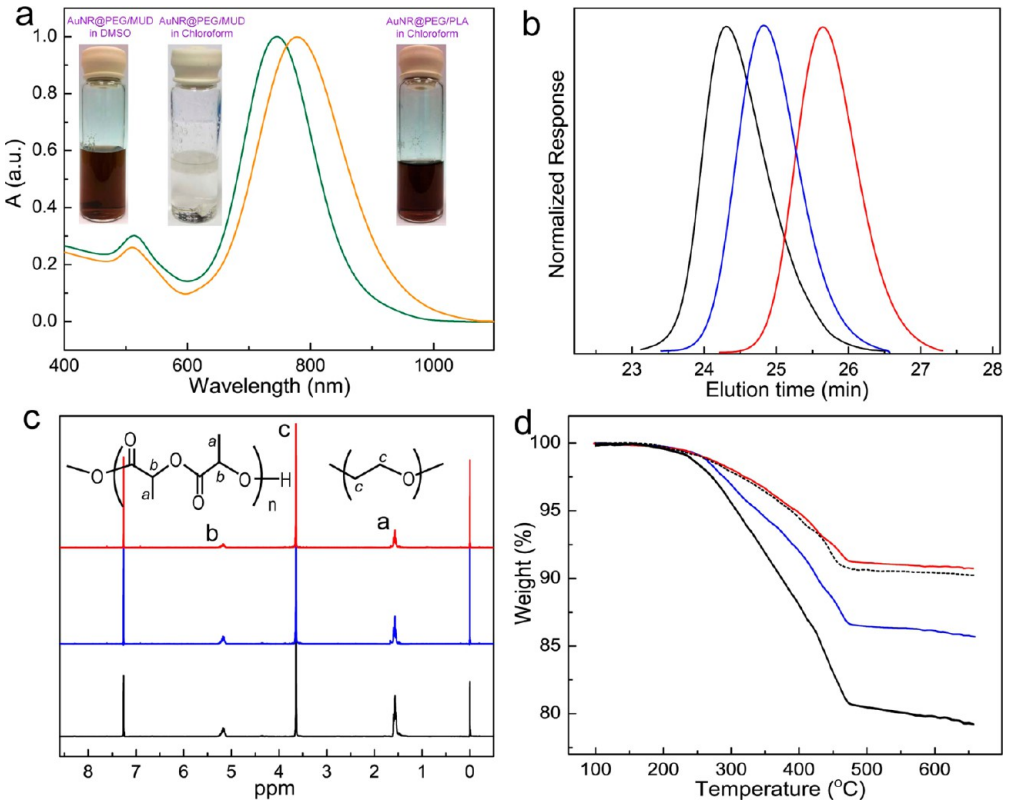

Figure 2. (a) UV−vis spectra of AuNRs coated with CTAB in water (green line) and AuNR@PEG/PLA in chloroform (orange line). Inset: photographs of AuNRs coated with PEG, MUD, and NPT (AuNR@PEG/MUD) in DMSO (left) and chloroform (middle) and AuNR@PEG/PLA in chloroform (right). (b) GPC traces of the PLA detached from AuNR@PEG/PLA with different molecular weights. ^{1}H NMR (c) and TGA (d) analysis of the AuNR@PEG/PLA with different molecular weight PLAs (red line, M_n = 6.5 kDa; blue line, M_n = 13 kDa; black line, M_n = 21 kDa) and AuNR@PEG/PLA prepared by one -step ligand exchange reaction using thiolated PEG (M_n = 5 kDa) and PLA (M_n = 21 kDa) (dash line).

same molecular weight led to a graft density of 0.25 chain/nm^2, which is only 50% (Figure 2d) of what we obtained through the tandem "grafting to" and "grafting from" method. Polymer coatings have been widely used to improve colloidal stability and biocompatibility of functional nanocrystals. Polymer brushes with a higher graft density can offer better shielding of the hard "core", which is certainly beneficial for these functions. Furthermore, a dense layer of amphiphilic mixed polymer brushes is also highly desirable in the amphiphilicity-driven self-assembly because self-association of hydrophobic grafts, regulated by hydrophilic ones to prevent the formation macroscopic aggregates, provide driving force for the self-assembly in aqueous media. In "grafting to" reactions, polymer grafts attached initially generate steric hindrance to block the attachment of incoming chains, therefore leading to low graft densities. This effect becomes more prominent for polymer grafts of higher molecular weights, making it difficult to flexibly control essential parameters of polymer brushes such as molecular weight and graft densities. And the loading of mixed polymer brushes introduces additional complexity of competition between the chemically different polymer chains during ligand exchange reaction. Our strategy overcomes this problem by loading mixed amphiphilic brushes sequentially in tandem "grafting to" and "grafting from" reactions, allowing for tailoring the structure of mixed brushes in a broad range. Particularly, the development of surface-initiated living organocatalytic ROP on functional nanocrystals expand the possible library of polymer brushes that can be structurally integrated with nanocrystals, opening synthetic approaches to imparting new functionalities such as biodegradability to the hybrid nanomaterials.

Amphiphilic AuNR@PEG/PLA ($M_{n(PLA)}$ = 13.0 kDa) were assembled into vesicles using the film rehydration method we reported previously.[24] Scanning electron microscopy (SEM) image (Figure 3a) reveals vesicles of ~190 nm in size (Figure S3) with AuNRs horizontally oriented along the vesicle shell. The clear contrast between the interior and peripheral region in the vesicles, observed in transmission electron microscopy (TEM) (Figure 3b), confirms the presence of hollow cavity in the vesicles. In comparison with the typical collapsed structures observed in dried polymeric vesicles, the plasmonic vesicles with embedded nanorods in the polymer shell maintained their structural integrity after dried, appearing to exhibit better mechanical stability. The close attachment of AuNRs in the vesicles leads to strong interparticle plasmonic coupling, as evidenced by the significant red-shift of

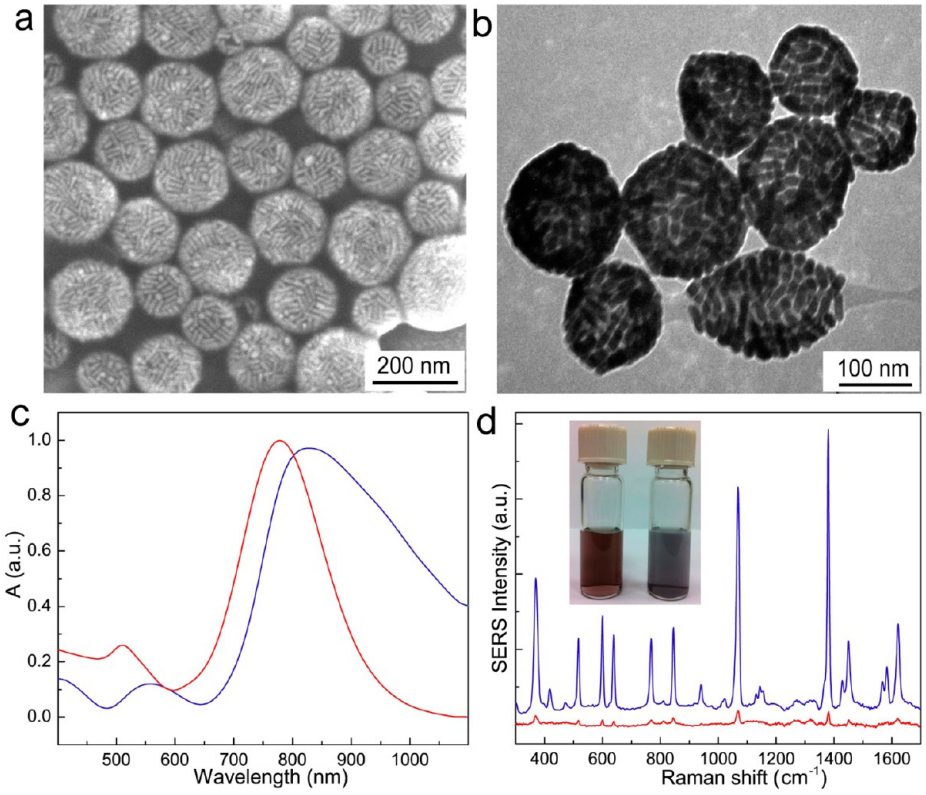

Figure 3. SEM (a) and TEM (b) images of the AuNR@PEG/PLA plasmonic vesicles. (c) UV−vis spectra of the AuNR@PEG/PLA in chloroform (red line) and the plasmonic vesicles in water (blue line). (d) SERS spectra of the AuNRs (red line) and plasmonic vesicles (blue line) and corresponding photographs of AuNR (left) and plasmonic vesicle (right) dispersion (Inset).

transverse and longitudinal LSPR of AuNRs (Figure 3c). Our synthetic strategy allows for the growth of well-defined mixed polymer brushes on nanoparticle scaffolds synthesized in established wet-chemical methods, which enables us to precisely tailor the optical properties of assembled vesicles for biological applications. Here we purposely adjusted the LSPR wavelength of the plasmonic vesicles to match the laser wavelength (808 nm) for maximal photothermal conversion efficiency. The degree of plasmonic coupling of AuNRs in the vesicle is strongly dependent on the relative ratio of PEG and PLA, which can be controlled by changing the relative ratio of PEG and MUD in the ligand exchange reaction. It was found that increasing the PLA/PEG ratio to 3.5 and 4.5, while maintaining the same graft density, caused further red-shift of the longitudinal LSPR to 883 and 940 nm (Figure S4). We reason that reducing the number of PEG grafts minimizes the steric hindrance for the association of AuNRs during the self-assembly and gives rise to more efficient packing of the nanorods and consequently stronger plasmonic coupling. AuNRs encoded with NPT Raman probes through Au−S bond exhibit SERS activity (Figure 3d) when excited with 785 nm laser. And the SERS signal (Figure 3d) is further enhanced by a factor of 24 due to the strongly coupled AuNRs in the vesicles, resulting in an overall enhancement factor of 5.7×10^6 (see details in Supporting Information).

Enzymatic Degradation and Photothermal Properties of the Amphiphilic Vesicles of AuNR@PEG/PLA. We further examined biodegradability of the AuNR@PEG/PLA vesicles by treating them with proteinase K, which is among the most active enzymes to degrade PLA.[53,54] Complete degradation of hydrophobic PLA converts it into water-soluble lactic acid and is expected to change the structural integrity and morphology of the plasmonic vesicles. After a treatment of 5 h at 37 °C, SEM image (Figure 4a) clearly shows that small holes appeared in the originally intact vesicles (Figure 2a) with their hollow cavities exposed. At 15 h, defects between individual AuNRs became more evident and major fragments falling off the vesicles were seen, indicative of homogeneous degradation of the PLA shell. Further extension of the treatment to 25 h led to collapse of the majority of vesicles, suggesting a major loss of the PLA component. Eventually, at 35 h, mostly small clusters of AuNRs rather than defected vesicles were observed. To further confirm the disruption of the vesicle was caused by the enzyme, control experiments were performed in pH 7.4 PBS and pH 5.0 acetate buffer in absence of proteinase K. After incubation at 37 °C for 45 h, the substantial degradation of vesicles appearing in presence of the enzyme was not observed and the vesicle structure was retained (Figure S5a,b), consistent with the stability of PLA for more than 15 days under these conditions.[29]

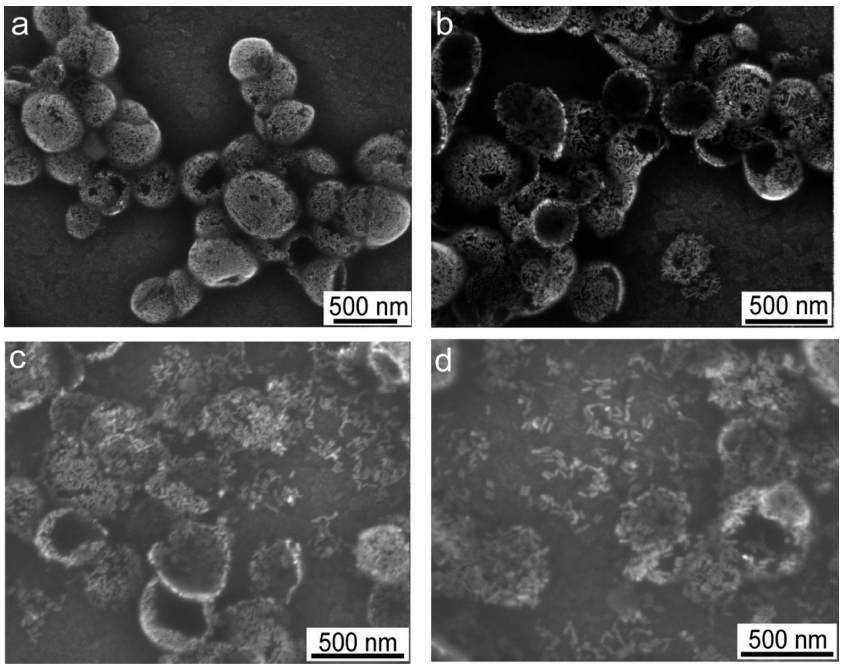

Figure 4. SEM images of the vesicles after treatment by the enzyme for 5 h (a), 15 h (b), 25 h (c), and 35 h (d).

We next investigated the impact of enzymatic degradation on controlled release of the payload encapsulated in the vesicles. Anticancer drug doxorubicin (DOX) was loaded in the vesicles by dissolving deprotonated DOX together with AuNR@PEG/PLA in chloroform to prepare the thin film for rehydration with pH 10.0 $NaHCO_3$ buffer.[37] In line with our previous study, our results (Figure 5a) show that increasing the amount of DOX added results in continuous rise of loaded DOX in the vesicles up to 58%; however, the loading efficiency drops after the feeding weight ratio of DOX and vesicle goes beyond 25%. Fluorescence of DOX was significantly quenched after encapsulation (Figure 5b), possibly because of the quenching and absorption of fluorescence by AuNRs in the vesicles. Generation of structural defects on the vesicle shell by enzymatic degradation is expected to cause the release of payload encapsulated in the vesicle. We have found that enzymatic treatment of DOX-loaded AuNR@PEG/PLA vesicle led to gradual recovery of DOX fluorescence (Figure 5c) up to 80% at 35 h, indicating the release of DOX into aqueous medium. And no significant DOX fluorescence was recovered after the treatment in either pH 7.4 PBS or pH 5.0 acetate buffer for 45 h (Figure S5c,d). The release kinetics of DOX was determined by measuring the absorption of free DOX at 485 nm after removing the vesicles by centrifugation. While a cumulative DOX release of 86% was achieved after enzymatic treatment of 45 h (Figure 5d), the release of DOX at pH 7.4 and 5.0 buffer dispersions was exceedingly slow, and only reached 9% at pH 7.4 and 14% at pH 5.0 after 45 h, agreeing well with the slow vesicle degradation observed in SEM observation and also suggesting stable trapping of DOX. However, it is noticed that enzyme treatment only caused 8% release in the first 5 h, although small holes of about 20−50 nm already appeared on the vesicles after 5 h degradation. We reason that the holes could be generated under the high vacuum condition during SEM experiments when the structure stability of vesicles is compromised after partial PLA degradation. Otherwise, shell defects in this size scale are expected to cause much faster payload release.

The photothermal conversion property of AuNR@PEG/PLA was evaluated by infrared thermographic mapping. As shown in Figure 6a, temperature of the vesicle dispersion (0.05 nM AuNRs) underwent a rapid increase to more than 60 °C in 20 min under the irradiation of 808 nm diode laser at a power output of 2.5 W/cm^2. In contrast, very minor temperature change (<3 °C) was detected for the control PBS buffer, suggesting highly efficient photothermal conversion of the plasmonic vesicles. Also noted is better performance (Figure 6b) of the vesicles than AuNRs at the same concentration, which should result from the precise matching of the longitudinal LSPR of the vesicles with the laser wavelength (808 nm) (Figure 3c). The comparison of the vesicles and nanorods at different laser power output showed the same trend (Figure 6c), with higher power affording faster temperature increase. In SEM and TEM images (Figure 6d,e), spherical vesicles were transformed into flattened pancake-like clusters of AuNRs after an irradiation of 6 min, further confirming the rapid generation of a tremendous amount of heat during laser exposure. The large optical cross-section (>10^9 M^{-1} cm^{-1}) of plasmonic nanostructures in the NIR spectral range contributes to their superior performance in localized heating.[55,56] We also examined the impact of such a

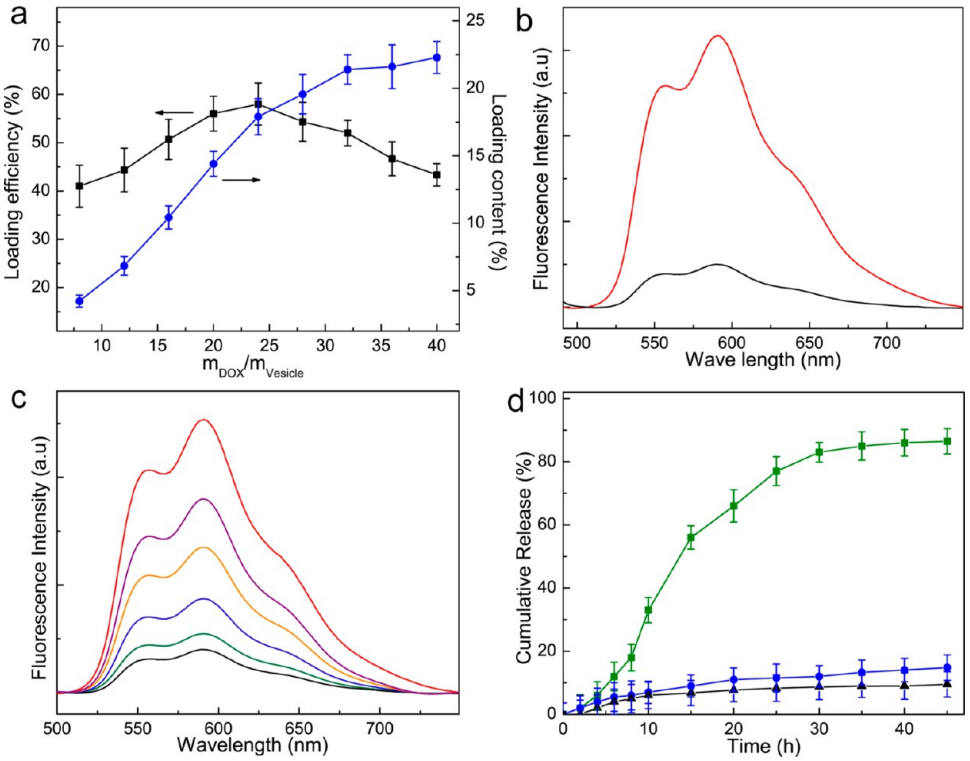

Figure 5. (a) DOX loading efficiency (black line) and loading content (blue line) in the plasmonic vesicles as a function of the feeding ratio of DOX *versus* the vesicle. (b) Fluorescence spectra of free DOX (red line) and DOX-loaded vesicles (black line) at the same DOX concentration. (c) Fluorescense spectra of DOX (red line) and DOX-loaded vesicle at the same DOX concentration after different times of enzymatic degradation: 0 h (black line), 5 h (green line,) 15 h (blue line), 25 h (orange line), and 35 h (purple line). (d) Typical *in vitro* release profiles of DOX-loaded vesicles in PBS with enzyme (green line), pH 5.0 acetate buffer (blue line), and pH 7.4 PBS (black line) at 37 °C.

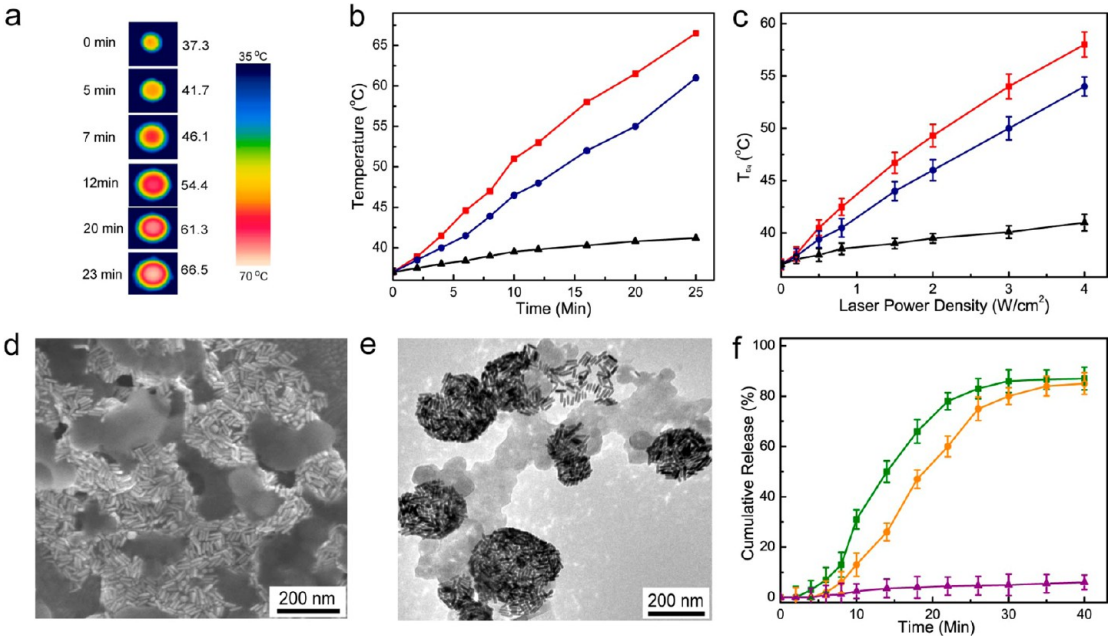

Figure 6. (a) Infrared thermographic images of vesicle dispersions in 96-well plate irradiated by a diode laser (808 nm) at a power output of 2.5 W/cm^2. (b) Temperature variation of vesicles (red line), AuNRs (blue line), and PBS (black line) as a function of laser irradiation time at 2.5 W/cm^2. (c) Plotted average temperatures at different power density laser irradiation: vesicle (red line), AuNR (blue line), and PBS (black line). SEM (d) and TEM (e) images of the vesicles after 6 min laser irradiation at 2.5 W/cm^2. (f) DOX release profiles of DOX-loaded vesicles without (purple line) and with laser at 1.0 W/cm^2 (orange line) and 2.5 W/cm^2 (green line) for 8 min irradiation.

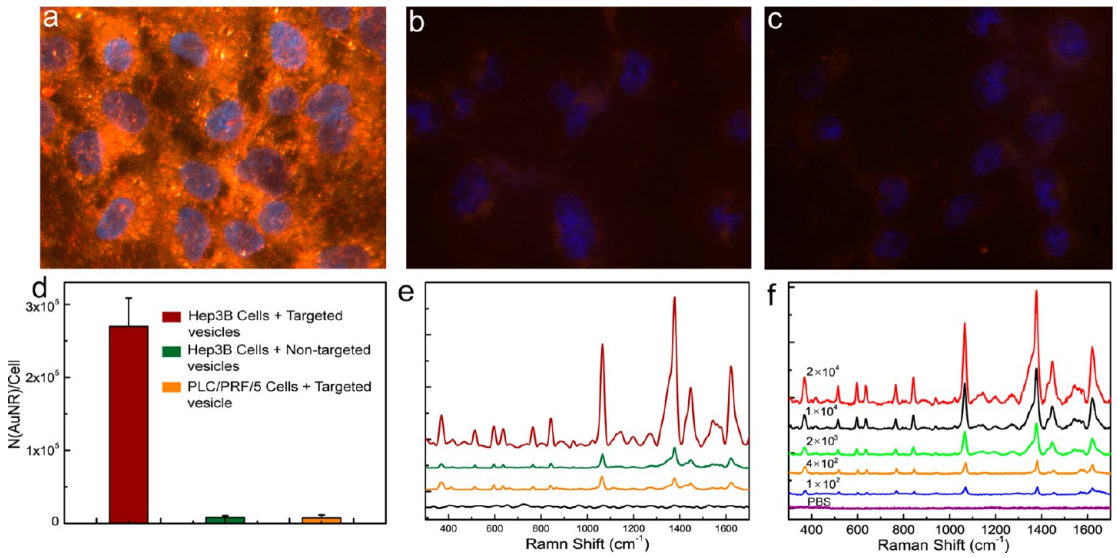

Figure 7. Overlaid dark-field and fluorescence images of live Hep3B cells incubated with targeted vesicles (a) and nontargeted vesicles (b), and live PLC/PRF/5 cells cultured with targeted vesicles (c). Cell nuclei were stained with blue fluorescent Hoechst 33342. (d) The average number of AuNRs uptake by cancer cells under different conditions. (e) SERS signals of Hep3B cells incubated with targeted vesicles (brown line) and nontargeted vesicles (green line), PLC/PRF/5 cells treated with targeted vesicles (orange line), and control Hep3B cells (black line). (f) SERS spectra of different concentrations (number of cells/mL) of Hep3B cells labeled with targeted vesicles.

dramatic structural change on payload release from the vesicles. AuNR@PEG/PLA vesicle dispersion was exposed to 808 nm laser at the power output of 1.0 and 2.5 W/cm^2 for 8 min and then the release of DOX was monitored over a period of 40 min. The vesicle showed minimal drug release in absence of laser irradiation. And over 85% of DOX was released in 30 min after laser exposure at 2.5 W/cm^2 and it dropped to 80% at 1.0 W/cm^2 (Figure 6f). This result is in line with the considerable vesicle disruption by localized heating observed in SEM and TEM images (Figure 6d,e). The availability of both slow enzymatic degradation and acute photothermal disruption of Au@PEG/PLA vesicles provides possibilities for personalizing the payload release kinetics in practical applications, where long-term stability allows for retaining the payload before the vesicles reach targeted tissue and photoactivated rapid release can create a localized high dosage to maximize the therapeutic efficacy. In thermotherapy, cells at 42−45 °C become more sensitive to the treatment of chemotherapy and radiation.[57] The efficient photothermal conversion of AuNR@PEG/PLA vesicle, in conjugation to its drug loading capacity, makes it a promising nanomedicine platform that can take full advantage of this effect for combination therapy.

Targeting and Spectroscopic Detection of Cancers Cell by Bioconjugated AuNR@PEG/PLA Vesicles. To explore the use of SERS-active AuNR@PEG/PLA vesicles for spectroscopic detection of specific cancer cells, in the "grafting to" reaction, we replaced 35% of the monofunctional thiolated PEG with heterofunctional PEG ended with thiol and carboxylic acid groups for the bioconjugation of targeting ligands. Here, monoclonal antibodies against epithelial cell adhesion molecule (EpCAM),[58,59] which is highly overexpressed in varieties of human cancer of epithelial origin, were tagged on the vesicles by 1-ethyl-3-(3-dimethylaminopropyl)carbodiimide (EDAC) catalyzed coupling. The dense layer of PEG on the surface of the vesicles plays multifunctional roles in improving the colloidal stability in cell culture medium and minimizing nonspecific cell uptake, in addition to serve as flexible spacer of the targeting ligands. We have chosen two hepatocellular carcinoma (HCC) cell lines, *i.e.*, EpCAM-positve Hep3B and EpCAM-negative PLC/PRF/5 cells (Figure S6) in this study. HCC is currently the fifth most common cancer type and the no. 3 killer in all cancer-related deaths, accounting for over 600 000 deaths every year.[60] The strong scattering of AuNRs at their LSPR wavelength allows for imaging the cellular binding and intracellular distribution of the plasmonic vesicles by dark-field microscopy. As displayed in Figure 7, 40 min of incubation gave rise to considerable uptake of the bioconjugated vesicles by the EpCAM-positve Hep3B cells, whereas the control vesicles without antibody ligand showed little cellular uptake by the Hep3B cells. Similarly, very weak scattering signal of the targeted vesicles (Figure 7c) was detected in the EpCAM-negative PLC/PRF/5 cells. Inductively coupled plasma mass spectroscopy (ICP-MS) analysis was further performed to make quantitative comparison. Figure 7d revealed that the total amount of AuNRs (2.7×10^5) taken up by the Hep3B cells incubated with targeted vesicles was about 33 times higher than that (8.2×10^3) of nontargeted control samples, which is very close to the amount in PLC/PRF/5 cells. Raman spectroscopic detection also showed highly specific labeling of Hep3B cells by the targeted vesicles against negative controls (Figure 7e). In comparison

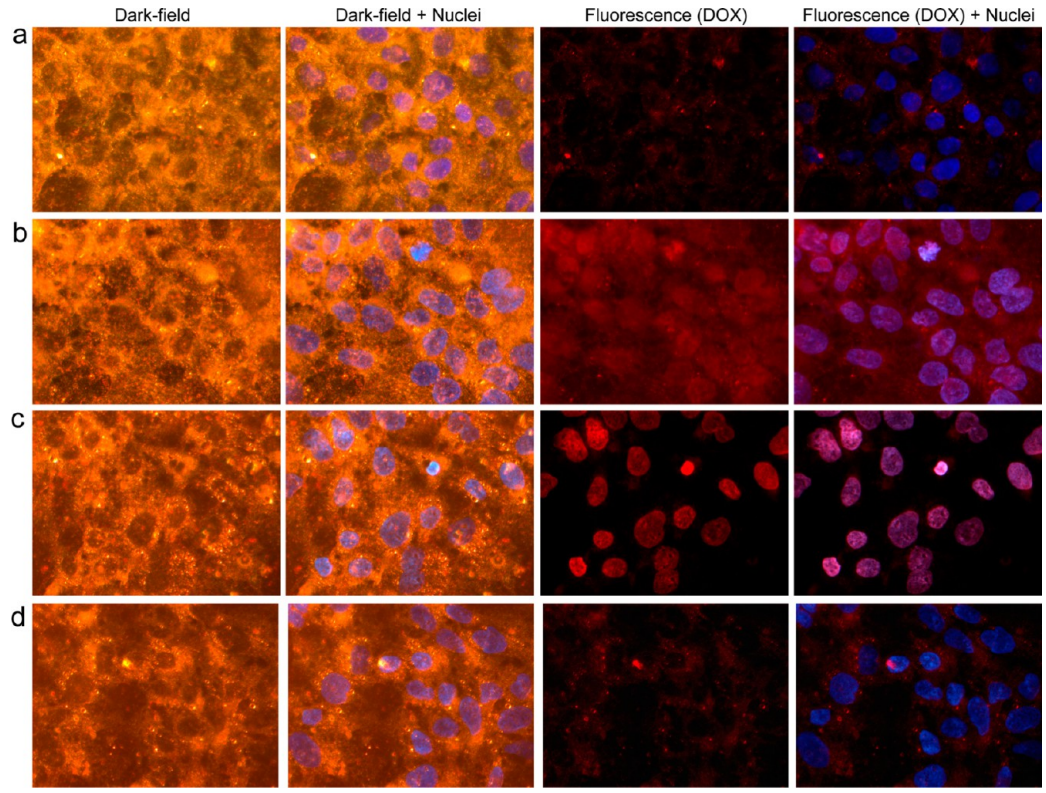

Figure 8. Dark-field, fluorescence and the overlaid images of Hep3B cells labeled with bioconjugated DOX-loaded vesicles after 40 min incubation (a), postincubation for 30 min (b) and 60 min (c) after laser irradiation at 1.0 W/cm^2 for 8 min, and 48 h postincubation without laser irradiation (d). DOX has a red fluorescence and cell nuclei were counter-stained with Hoechst 3342 exhibiting blue fluorescence.

with commonly used fluorescence probes, SERS-encoded nanoprobes offer a number of advantages such as low background signals, better photostability, and tremendous potential for multiplexing that are highly important for biosensing of molecular, cellular, and *in vivo* targets.[61] To evaluate the sensitivity of our SERS-encoded plasmonic vesicles, a series of labeled Hep3B cells was subjected to Raman spectroscopic measurements, which revealed a low detection limit of 40 cells/mL (Figure 7f and Figure S7), demonstrating the potential of detecting satellite tumor nodules and tiny metastasis *in vivo*.

Combined Dual-Modality Chemo-Photothermal Therapy by AuNR@PEG/PLA Vesicles. Active targeting of DOX-loaded AuNR@PEG/PLA vesicles to EpCAM-positve cells enables the laser-activated intracellular release of DOX. Dual-modality dark-field and fluorescence microscopy was used to monitor the delivery process by independently tracking the plasmonic vesicles and red fluorescence of DOX. Figure 8a shows that weak fluorescence of DOX was detected and largely co-localized with the vesicles after an incubation of 40 min. However, stronger red fluorescence, homogeneously distributed throughout the cells, was observed 30 min after a laser irradiation (1.0 W/cm^2) of 8 min, with the plasmonic scattering remaining unchanged. As discussed above, fluorescence of DOX was significantly quenched after encapsulation, but recovered once it is released from the vesicles. The change of DOX fluorescence intensity and intracellular distribution implies laser-activated release of DOX, which is further supported by nucleus-accumulation of DOX (Figure 8c) at 60 min after laser exposure. In contrast, without laser irradiation, the plasmonic and fluorescence signals did not show any change after 48 h of incubation (Figure 8d), indicating the stable encapsulation of DOX and the absence of highly active proteinase or esterase for PLA degradation in the local environment, which is consistent with the *in vitro* and *in vivo* degradation kinetics of PLA reported previously.[29,62,63]

Tailoring the laser power output to induce cytotoxic heat allows us to investigate the combination cancer therapy with integrated photothermal therapy and chemotherapy. A live/dead assay, with calcein AM staining live cells and propidium iodide (PI) highlighting dead/late apoptotic cells, reveals that the photothermal effect of targeted AuNR@PEG/PLA vesicles under cell-tolerable laser exposure (1.0 and 2.5 W/cm^2) yields power-dependent cell death (Figure 9a). And the cytotoxic effect was further enhanced when DOX is loaded into the vesicles. It appears that a mild laser irradiation (1.0 W/cm^2), in conjuction with a low dosage of DOX (0.5 μg/mL), is sufficient to cause almost 100% death of Hep3B cells by the EpCAM-targeted vesicles. In contrast, the nontargeted vesicles showed minimal

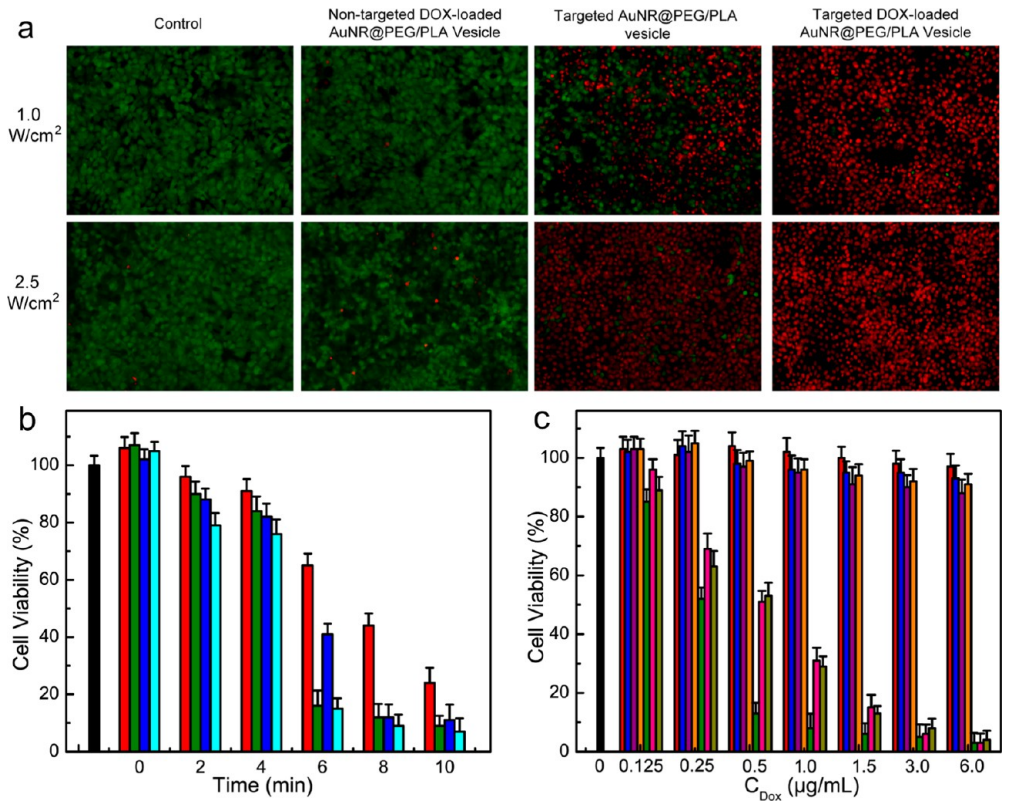

Figure 9. (a) Fluorescence images of Hep3B cancer cells after chemo-photothermal therapy with nontargeted DOX-loaded vesicles, targeted vesicles and targeted DOX-loaded vesicles irradiated by a laser (808 nm) at a power output of 1.0 or 2.5 W/cm^2 for 8 min. Cells were stained with calcein AM (live, green) and PI (dead, red) after 24 h postincubation. Control: laser only. (b) Viability of Hep3B cells incubated with targeted blank vesicle exposed to 1.0 W/cm^2 (red bar) and 2.5 W/cm^2 (blue bar) laser, and targeted DOX-loaded vesicle exposed to 1.0 W/cm^2 (green bar) and 2.5 W/cm^2 (cyan bar) for different times laser irradiation. (c) Viability of Hep3B cells incubated targeted vesicle (red bar), nontargeted DOX-loaded vesicle without (blue bar) and with laser (purple bar) (power output, 1.0 W/cm^2; irradiation time, 8 min), targeted DOX-loaded vesicle without (orange bar) and with laser (green bar), free DOX without (pink bar) and with laser (dark yellow bar) at different concentrations of DOX.

cytotoxicity under the same treatment condition (Figure 9a), which is consistent with the dramatic difference in cellular uptake measured by imaging, SERS spectroscopy, and ICP-MS.

To quantitatively evaluate the therapeutic efficacy of the DOX-loaded plasmonic vesicle, viability of corresponding Hep3B cells was measured using cell-counting kit-8 (CCK-8). Biocompatibility of the AuNR@PEG/PLA vesicles was manifested by the fact that the targeted vesicles showed no toxicity 24 h after uptake by Hep3B cells (Figure 9b). When the laser exposure time is shorter than 4 min, both the targeted blank vesicles and vesicles containing drug affords similar low toxicity (<25%), indicating little release of DOX after a short period of laser exposure and a primary contribution by photothermal heat. However, a considerably better therapeutic effect (>160%) of drug-loaded vesicles than that of the blank vesicles was observed after 8 min irradiation at 1.0 W/cm^2, suggesting the initiation of DOX release and a combined chemo-photothermal therapy. On the other hand, exposure to 2.5 W/cm^2 laser for 8 min led to more than 80% cell death, which is similar to what is caused by the drug-loading vesicles, indicative of the generation of a tremendous amount of cytotoxic heat at higher power output. As shown in Figure 9c, targeted vesicle and targeted DOX-loaded vesicle without laser induced negligible toxicity, while the targeted DOX-loaded vesicles with laser and free DOX caused dose-dependent cytotoxicity. In case of DOX delivered by targeted vesicles, the combination of hyperthermia therapy from vesicles and chemotherapy of DOX reduced half maximal inhibitory concentration (IC_{50}) of DOX from 0.49 μg/mL of free DOX to 0.26 μg/mL, leading to a synergistic therapeutic effect that is considerably better than that of individual treatment. Taken together, the effective localized heating and resultant drug delivery can give rise to the synergistic treatment of specific cancer cells, which, in conjugation with SERS-based ultrasensitive spectroscopic detection, make biodegradable plasmonic vesicles a promising theranostic platform. Accumulating evidence has demonstrated an urgent need in combination therapy that integrates the therapeutic effects of multiple reagents or mechanisms to improve the treatment of highly heterogeneous human cancer.[50,64] In light of the recent development in Raman spectrometers for intraoperative applications,[46] biodegradable plasmonic vesicles

that allow for personalized photoactivated payload release are of great potential for the integrated detection and chemo-photothermal treatment of positive tumor margins and micrometastases during cancer surgery, which are primary causes of cancer resurgence.

CONCLUSION

In summary, we have realized surface initiated organocatalytic ROP on functional nanocrystals, which enabled the synthesis of amphiphilic AuNRs covered with well-defined mixed PEG and PLA brushes. Self-assembly of amphiphilic AuNR@PEG/PLA give rise to plasmonic vesicles consisting of PEG corona and AuNRs-embedded PLA shell, which endow the vesicles with a unique combination of structural and optical properties such as high colloidal stability, excellent biocompatibility, enzymatic biodegradability, and photothermal disruption. One key finding is that SERS-active plasmonic vesicles, tagged with cancer targeting ligands, can function as a new class of theranostic platform that allows for simultaneous SERS detection and synergistic chemo-photothermal therapy of specific cancer cells. The versatile chemistry of organocatalytic ROP, in conjugation with recent development in wet-chemical synthesis of functional nanocrystals with tailored optical, electronic, and magnetic properties, opens new possibilities for constructing a new generation of biodegradable theranostic platforms for clinical translation.

EXPERIMENTAL SECTION

Materials and Characterization. 11-Mercapto-1-undecanol (MUD), 2-naphthalenethiol (NPT), doxorubicin (DOX), 4-dimethylaminopyridine (DMAP), D,L-lactide (LA), triethylamine (TEA), cetyltrimethylammonium bromide (CTAB), sodium borohydride ($NaBH_4$), silver nitrate ($AgNO_3$), 2-(2-aminoethoxy)ethanol, 1-ethyl-3-(3-dimethylaminopropyl) carbodiimide (EDAC), propidium iodide (PI), and proteinase K were purchased from Sigma-Aldrich. LA was recrystallized from dry ethyl acetate three times. All solvents unless specified were obtained from Sigma-Aldrich and used as received. Methoxy-poly(ethylene glycol)-thiol (MPEG-SH) and carboxyl-poly-(ethylene glycol)-thiol (HOOC-PEG-SH) with a molecular weight of 5 kDa were received from Laysan Bio. Hydrogen tetrachloroaurate-(III) trihydrate ($HAuCl_4 \cdot 3H_2O$) was from Alfa Aesar. Hoechst 3342 and calcein AM were purchased from Life technology.

Scanning electron microscopy images were obtained on a FESEM (JSM-6700F, Japan). Transmission electron microscopy (TEM) observations were conducted on a Jeol JEM 2010 electron microscope at an acceleration voltage of 300 kV. UV−vis absorption spectra were recorded by using a Shimadzu UV-2501 spectrophotometer. ^{1}H NMR spectra were obtained at Bruker AV300, using dimethyl sulfoxide-d_6 (DMSO-d_6) and $CDCl_3$ as solvents. Gel permeation chromatography (GPC) was measured on a Shimadzu HPLC system using chloroform as the eluent, and the molecular weight is calibrated with polystyrene standards. PEG and MUD, and polymer grafts were cleaved from AuNRs by treating the nanorods with 5 mM iodine solution in chloroform,[65,66] and PLA was separated from PEG by precipitating the solution in water. Fluorescence spectra were collected on a Fluoromax-3 spectrometer (Horiba Scientific). Dark-field imaging of live cells were carried out in an Olympus71 inverted microscope with an oil-immersion dark-field condenser at 40× magnification, and fluorescence images were collected using Photometrics CoolSNAP-cf cooled CCD camera. Infrared thermographic images of vesicle dispersions were obtained using FLIR T420 thermal imaging infrared camera. Live cells were immobilized on a polylysine-modified glass coverslip for the imaging experiments. Inductively coupled plasma mass spectroscopy (ICP-MS) was measured on a Prodigy High Dispersion ICP-MS. Hydrodynamic sizes were measured using a Malvern NANO-ZS90 Zetasizer. Thermogravimetric analysis (TGA) was performed on a Perkin-Elmer Diamond TG/DTA. Samples were placed in platinum sample pans and heated under a nitrogen atmosphere at a rate of 10 °C/min to 100 °C and held for 40 min to completely remove residual solvent. Samples were then heated to 700 °C at a rate of 10 °C/min. A CW diode laser of 808 nm (spot size: 1 cm) was used for the laser irradiation experiment. A RENISHAW Raman microscope with WIRE 2.0 software and 785 nm emission line of an air-cooled He−Ne laser was used for SERS measurements. The laser beam was focused by a 50× objective, and the laser power on samples was 0.45 mW with a laser spot size of 2−5 μm. A single scan with an integration time of 15 s was performed. The encoder feedback controlled the grating stage with a holographic grating of 1800 lines/mm on an interchangeable magnetic mount.

Synthesis of SERS-Active Amphiphilic AuNRs with Mixed Polymer Brushes of PEG and PLA. CTAB stabilized AuNRs were synthesized using a seed-mediated method,[67] and free CTAB were removed by repeated centrifugation (9000*g*, 20 min). A total of 0.1 mL 2-(2-aminoethoxy)ethanol was slowly added into 4 mL AuNR dispersion (30 nM) and the mixture was stirred for 12 h. The modified AuNRs were obtained by centrifugation (9000*g*, 10 min) and dispersed in 4 mL DMSO. The amphiphilic AuNRs with polymer brushes of PEG and PLA were synthesized by tandem "grafting to" and "grafting from" reactions. In the first step, 1 mL of DMSO solution of 40 mg of PEG (HOOC-PEG-SH and MPEG-SH with a molar ratio of 35/65), 6.5 mg of MUD and 0.12 mg of NPT was added into the AuNR dispersion over 10 min, and the mixture was stirred for 12 h before the sample was precipitated in chloroform to remove unbound ligands. The obtained SERS-encoded AuNRs with PEG and MUD was suspended in 5 mL of anhydrous chloroform. In the "grafting to" step, 1.5 g of LA and 10 mg of DMAP were added into the obtained chloroform suspension of AuNR@PEG/MUD. After the reaction mixture was degassed with nitrogen for 40 min, the polymerization of LA was carried out at 40 °C. After a predetermined period of time, the AuNRs coated with PEG and PLA (AuNR@PEG/PLA) were separated from the mixture by centrifugation and purified by repeated redispersion and centrifugation in 2 mL of chloroform. To obtain Au@PEG/PLA with PEG/PLA ratio of 1:3.5 and 1:4.5, the ratio of PEG/MUD used in the ligand exchange reaction was adjusted to 5:28 and 5:37, respectively.

Fabrication of DOX-Loaded and Bioconjugated AuNR@PEG/PLA Vesicles. To prepare DOX-loaded vesicles, 120 μg of DOX was deprotonated with equal molar amount of TEA and dispersed in chloroform. Afterward, AuNR@PEG/PLA (30 nM AuNR) and DOX in 0.2 mL of chloroform were dried on a 4 mL glass vial wall to form a film, and then 1 mL of pH 10.0 $NaHCO_3$ buffer was added to rehydrate the film under sonication. The free DOX was removed by centrifugation and the obtained DOX-loaded vesicle was redispersed in pH 7.4 PBS for further use. The blank vesicle was prepared in the same condition except using water to rehydrate the AuNR@PEG/PLA film. To conjugate EpCAM antibody on the vesicles, antibody (400 μg) and EDAC (0.6 mg) were added into 1 mL of AuNR@PEG/PLA vesicle (0.1 nM AuNR) aqueous dispersion and the reaction was carried out at 4 °C for 8 h. The unconjugated antibody was removed by centrifugation (2000*g*, 5 mim) twice and the bioconjugated AuNR@PEG/PLA vesicles were stored in PBS at 4 °C.

Enzymatic Degradation of Plasmonic Vesicles and Triggered Drug Release. To test the vesicle degradation by enzyme, 1 mL of DOX-loaded vesicle (0.05 nM AuNR) dispersion incubated with 50 μL of proteinase K (25 mg/mL in Tris-HCl buffer, 800 U/mL activity) was loaded into a membrane dialysis tube with a

molecular cutoff of 3000 Da. The tube was immersed in a 20 mL glass bottle filled with 10 mL of pH 7.4 PBS buffer at 37 °C for 45 h. Control experiments were performed in pH 7.4 PBS and pH 5.0 acetate buffer without enzyme. DOX was quantified using its absorbance at 485 nm.

NIR Laser Irradiation and Triggered DOX Release. A total of 100 μL AuNR@PEG/PLA vesicle and AuNR dispersions (0.05 nM) in 96-well plate were irradiated with a 808 nm diode laser (spot size: 1 cm) at a power density of 1.0 and 2.5 W/cm^2 for 2−14 min. Temperature and thermographic images were taken by an infrared thermographic camera at 2 min intervals. For laser triggered DOX release experiments, 1 mL of DOX-loaded vesicle solution was loaded into a membrane dialysis tube (cut-off: 3000 Da). The tube with DOX-loaded vesicle solution was immersed in a 20 mL tube filled with 10 mL of pH 7.4 PBS. The experiments were performed after laser exposure (1.0 or 2.5 W/cm^2) for 8 min at 37 °C. The amount of loaded and released DOX was determined by measuring the UV−vis absorbance of DOX at 485 nm. All measurements were conducted in triplicate.

Live Cell Imaging and SERS Detection. Hep3B cells and PLC/PRF/5 cells were transferred and cultured onto 60 mm polylysine-modified glass slides in culture dish and allowed to grow in DMEM medium supplemented with 10% fetal bovine serum and 1% antibiotics (37 °C, 5% CO_2) for 48 h. Next, the medium was replaced with fresh culture medium containing nontargeted vesicles (0.1 nM) for Hep3B cells and targeted vesicles (0.1 nM) for both Hep3B and PLC/PRF/5 cells. After incubation for 40 min, the glass slides were washed with PBS for live cell imaging. The dark-field image was captured with unpolarized white light illuminated through a dark-field condenser. In case of the intracellular DOX release studies, Hep3B cells were treated with targeted DOX-loaded vesicles (0.1 nM) for 40 min with cell nuclei counterstained with Hoechst 33342. To obtain the *in situ* disruption of the plasmonic vesicles inside live cells, cells were irradiated by an 808 nm laser at 1.0 W/cm^2 for 8 min. The cellular fluorescence images were collected using wide-band blue excitation (450−480 nm) provided by a mercury lamp, a long-pass dichroic filter (500 nm), and a band-pass emission filter (590−630 nm). Dark-field images were captured as described above. For SERS detection of targeted cancer cells, preseeded Hep3B cells were exposed to targeted vesicles for 40 min. Afterward, the cells were washed with PBS three times and collected after treated by trypsin. The obtained cells were counted and redispersed in 200 μL of PBS at different concentrations for the Raman detection.

Chemo-Photothermal Therapy of Hep3B Cells Labeled with Bioconjugated DOX-Loaded AuNR Vesicles. Hep3B cells were seeded in each well of 96-well plates at a density of 1.0×10^4 cells/well and incubated for 48 h. Afterward, the cells were exposed to targeted blank vesicles and targeted DOX-loaded vesicles at the same DOX concentration (0.5 μg/mL). After incubation for 40 min, the cells were washed with PBS and fresh medium was added. The cells were further irradiated with 808 nm laser at a power output of 1.0 and 2.5 W/cm^2 for 0, 2, 4, 6, 8, 10 min and incubated for 24 h before the cell viability was measured using the standard cell counting Kit-8 (CCK-8) assay. The data reported represent the means of triplicate measurements. In the live/dead assay, cells were stained with calcein AM (live, green) and propidium iodide (dead, red). In parallel, Hep3B cells were exposed to free DOX, nontargeted DOX-loaded vesicles, and targeted DOX-loaded vesicles at various DOX concentrations (0, 0.125, 0.25, 0.5, 1.0, 1.5, 3.0, 6.0 μg/mL) for 40 min. Afterward, cell culture medium was replaced with fresh one, and the cells were or were not irradiated with 808 nm laser at an output power of 1.0 W/cm^2 for 8 min. After cells were maintained in incubator for another 24 h, cell survival efficiency was measured using the CCK-8 assay.

Conflict of Interest: The authors declare no competing financial interest.

Supporting Information Available: Supporting data including TEM, SEM, and DLS measurements and structural analysis of the amphiphilic AuNRs and plasmonic vesicles; movie (.avi) that shows the organocatalytic ring-opening polymerization of lactide on AuNRs. This material is available free of charge *via* the Internet at http://pubs.acs.org.

Acknowledgment. H.D. thanks the Nanyang Assistant Professorship for financial support. This work is also supported by the INSIST program at Nanyang Technological University.

REFERENCES AND NOTES

1. Halas, N. J. Plasmonics: An Emerging Field Fostered by Nano Letters. *Nano Lett.* **2010**, *10*, 3816–3822.
2. Mayer, K. M.; Hafner, J. H. Localized Surface Plasmon Resonance Sensors. *Chem. Rev.* **2011**, *111*, 3828–3857.
3. Willets, K. A.; Van Duyne, R. P. Localized Surface Plasmon Resonance Spectroscopy and Sensing. *Annu. Rev. Phys. Chem.* **2007**, *58*, 267–297.
4. Kwon, S. G.; Hyeon, T. Colloidal Chemical Synthesis and Formation Kinetics of Uniformly Sized Nanocrystals of Metals, Oxides, and Chalcogenides. *Acc. Chem. Res.* **2008**, *41*, 1696–1709.
5. Tao, A. R.; Habas, S.; Yang, P. D. Shape Control of Colloidal Metal Nanocrystals. *Small* **2008**, *4*, 310–325.
6. Cobley, C. M.; Chen, J. Y.; Cho, E. C.; Wang, L. V.; Xia, Y. N. Gold Nanostructures: A Class of Multifunctional Materials for Biomedical Applications. *Chem. Soc. Rev.* **2011**, *40*, 44–56.
7. Srivastava, S.; Kotov, N. A. Nanoparticle Assembly for 1D and 2D Ordered Structures. *Soft Matter* **2009**, *5*, 1146–1156.
8. Grzelczak, M.; Vermant, J.; Furst, E. M.; Liz-Marzán, L. M. Directed Self-Assembly of Nanoparticles. *ACS Nano* **2010**, *4*, 3591–3605.
9. Nie, Z. H.; Petukhova, A.; Kumacheva, E. Properties and Emerging Applications of Self-Assembled Structures Made from Inorganic Nanoparticles. *Nat. Nano.* **2010**, *5*, 15–25.
10. Tan, S. J.; Campolongo, M. J.; Luo, D.; Cheng, W. Building Plasmonic Nanostructures with DNA. *Nat. Nanotechnol.* **2011**, *6*, 268–276.
11. Qian, X. M.; Nie, S. M. Single-Molecule and Single-Nanoparticle SERS: From Fundamental Mechanisms to Biomedical Applications. *Chem. Soc. Rev.* **2008**, *37*, 912–920.
12. Wang, Y.; Xu, J.; Wang, Y. W.; Chen, H. Y. Emerging Chirality in Nanoscience. *Chem. Soc. Rev.* **2013**, *42*, 2930–2962.
13. Qian, X. M.; Li, J.; Nie, S. M. Stimuli-Responsive SERS Nanoparticles: Conformational Control of Plasmonic Coupling and Surface Raman Enhancement. *J. Am. Chem. Soc.* **2009**, *131*, 7540–7541.
14. Yin, J.; Wu, T.; Song, J. B.; Zhang, Q.; Liu, S. Y.; Xu, R.; Duan, H. W. SERS-Active Nanoparticles for Sensitive and Selective Detection of Cadmium Ion (Cd^{2+}). *Chem. Mater.* **2011**, *23*, 4756–4764.
15. Choi, H. S.; Liu, W. H.; Misra, P.; Tanaka, E.; Zimmer, J. P.; Ipe, B. I.; Bawendi, M. G.; Frangioni, J. V. Renal Clearance of Quantum Dots. *Nat. Biotechnol.* **2007**, *25*, 1165–1170.
16. Peer, D.; Karp, J. M.; Hong, S.; Farokhzad, O. C.; Margalit, R.; Langer, R. Nanocarriers as an Emerging Platform for Cancer Therapy. *Nat. Nanotechnol.* **2007**, *2*, 751–760.
17. Wang, C. X.; Du, Y.; Wu, Q.; Xuan, S. G.; Zhou, J. J.; Song, J. B.; Shao, F. W.; Duan, H. W. Stimuli-Responsive Plasmonic Core-Satellite Assemblies: i-Motif DNA Linker Enabled Intracellular pH Sensing. *Chem. Commun.* **2013**, *49*, 5739–5741.
18. Nikolic, M. S.; Olsson, C.; Salcher, A.; Kornowski, A.; Rank, A.; Schubert, R.; Frömsdorf, A.; Weller, H.; Förster, S. Micelle and Vesicle Formation of Amphiphilic Nanoparticles. *Angew. Chem., Int. Ed.* **2009**, *48*, 2752–2754.
19. He, J.; Wei, Z.; Wang, L.; Tomova, Z.; Babu, T.; Wang, C.; Han, X.; Fourkas, J. T.; Nie, Z. Hydrodynamically Driven Self-Assembly of Giant Vesicles of Metal Nanoparticles for Remote-Controlled Release. *Angew. Chem., Int. Ed.* **2013**, *52*, 2463–2468.
20. Xu, J.; Zubarev, E. R. Supramolecular Assemblies of Starlike and V-Shaped PB−PEO Amphiphiles. *Angew. Chem., Int. Ed.* **2004**, *43*, 5491–5496.
21. Zubarev, E. R.; Xu, J.; Sayyad, A.; Gibson, J. D. Amphiphilic Gold Nanoparticles with V-Shaped Arms. *J. Am. Chem. Soc.* **2006**, *128*, 4958–4959.

22. Zubarev, E. R.; Xu, J.; Sayyad, A.; Gibson, J. D. Amphiphilicity-Driven Organization of Nanoparticles into Discrete Assemblies. *J. Am. Chem. Soc.* **2006**, *128*, 15098–15099.
23. Cheng, L.; Song, J. B.; Yin, J.; Duan, H. W. Self-Assembled Plasmonic Dimers of Amphiphilic Gold Nanocrystals. *J. Phys. Chem. Lett.* **2011**, *2*, 2258–2262.
24. Song, J. B.; Cheng, L.; Liu, A. P.; Yin, J.; Kuang, M.; Duan, H. W. Plasmonic Vesicles of Amphiphilic Gold Nanocrystals: Self-Assembly and External-Stimuli-Triggered Destruction. *J. Am. Chem. Soc.* **2011**, *133*, 10760–10763.
25. He, J.; Liu, Y.; Babu, T.; Wei, Z.; Nie, Z. Self-Assembly of Inorganic Nanoparticle Vesicles and Tubules Driven by Tethered Linear Block Copolymers. *J. Am. Chem. Soc.* **2012**, *134*, 11342–11345.
26. Hu, J. M.; Wu, T.; Zhang, G. Y.; Liu, S. Y. Efficient Synthesis of Single Gold Nanoparticle Hybrid Amphiphilic Triblock Copolymers and their Controlled Self-Assembly. *J. Am. Chem. Soc.* **2012**, *134*, 7624–7627.
27. Cheng, L.; Liu, A. P.; Peng, S.; Duan, H. W. Responsive Plasmonic Assemblies of Amphiphilic Nanocrystals at Oil−Water Interfaces. *ACS Nano* **2010**, *4*, 6098–6104.
28. Barbey, R.; Lavanant, L.; Paripovic, D.; Schüwer, N.; Sugnaux, C.; Tugulu, S.; Klok, H. A. Polymer Brushes *via* Surface-Initiated Controlled Radical Polymerization: Synthesis, Characterization, Properties, and Applications. *Chem. Rev.* **2009**, *109*, 5437–5527.
29. Tam, J. M.; Tam, J. O.; Murthy, A.; Ingram, D. R.; Ma, L. L.; Travis, K.; Johnston, K. P.; Sokolov, K. V. Controlled Assembly of Biodegradable Plasmonic Nanoclusters for Near-Infrared Imaging and Therapeutic Applications. *ACS Nano* **2010**, *4*, 2178–2184.
30. Ohno, K.; Koh, K. M.; Tsujii, Y.; Fukuda, T. Synthesis of Gold Nanoparticles Coated with Well-Defined, High-Density Polymer Brushes by Surface-Initiated Living Radical Polymerization. *Macromolecules* **2002**, *35*, 8989–8993.
31. Kim, J. B.; Bruening, M. L.; Baker, G. L. Surface-Initiated Atom Transfer Radical Polymerization on Gold at Ambient Temperature. *J. Am. Chem. Soc.* **2000**, *122*, 7616–7617.
32. Kamber, N. E.; Jeong, W.; Waymouth, R. M.; Pratt, R. C.; Lohmeijer, B. G. G.; Hedrick, J. L. Organocatalytic Ring-Opening Polymerization. *Chem. Rev.* **2007**, *107*, 5813–5840.
33. Xiong, M. H.; Bao, Y.; Yang, X. Z.; Wang, Y. C.; Sun, B.; Wang, J. Lipase-Sensitive Polymeric Triple-Layered Nanogel for "On-Demand" Drug Delivery. *J. Am. Chem. Soc.* **2012**, *134*, 4355–4362.
34. Xie, J.; Lee, S.; Chen, X. Nanoparticle-Based Theranostic Agents. *Adv. Drug Delivery Rev.* **2010**, *62*, 1064–1079.
35. You, J.; Zhang, G. D.; Li, C. Exceptionally High Payload of Doxorubicin in Hollow Gold Nanospheres for Near-Infrared Light-Triggered Drug Release. *ACS Nano* **2010**, *4*, 1033–1041.
36. Wang, F.; Wang, Y. C.; Dou, S.; Xiong, M. H.; Sun, T. M.; Wang, J. Doxorubicin-Tethered Responsive Gold Nanoparticles Facilitate Intracellular Drug Delivery for Overcoming Multidrug Resistance in Cancer Cells. *ACS Nano* **2011**, *5*, 3679–3692.
37. Song, J. B.; Zhou, J. J.; Duan, H. W. Self-Assembled Plasmonic Vesicles of SERS-Encoded Amphiphilic Gold Nanoparticles for Cancer Cell Targeting and Traceable Intracellular Drug Delivery. *J. Am. Chem. Soc.* **2012**, *134*, 13458–13469.
38. Lin, J.; Wang, S.; Huang, P.; Wang, Z.; Chen, S.; Niu, G.; Li, W.; He, J.; Cui, D.; Lu, G.; Chen, X.; Nie, Z. Photosensitizer-Loaded Gold Vesicles with Strong Plasmonic Coupling Effect for Imaging-Guided Photothermal/Photodynamic Therapy. *ACS Nano* **2013**, *7*, 5320–5329.
39. Otsuka, H.; Nagasaki, Y.; Kataoka, K. PEGylated Nanoparticles for Biological and Pharmaceutical Applications. *Adv. Drug Delivery Rev.* **2003**, *55*, 403–419.
40. Sinha Ray, S. Polylactide-Based Bionanocomposites: A Promising Class of Hybrid Materials. *Acc. Chem. Res.* **2012**, *45*, 1710–1720.
41. Kim, T. Y.; Kim, D. W.; Chung, J. Y.; Shin, S. G.; Kim, S. C.; Heo, D. S.; Kim, N. K.; Bang, Y. J.; Phase, I. and Pharmacokinetic Study of Genexol-PM, A Cremophor-Free, Polymeric Micelle-Formulated Paclitaxel, in Patients with Advanced Malignancies. *Clin. Cancer Res.* **2004**, *10*, 3708–3716.
42. Qian, X. M.; Peng, X. H.; Ansari, D. O.; Yin-Goen, Q.; Chen, G. Z.; Shin, D. M.; Yang, L.; Young, A. N.; Wang, M. D.; Nie, S. M. *In Vivo* Tumor Targeting and Spectroscopic Detection with Surface-Enhanced Raman Nanoparticle Tags. *Nat. Biotechnol.* **2008**, *26*, 83–90.
43. von Maltzahn, G.; Park, J. H.; Agrawal, A.; Bandaru, N. K.; Das, S. K.; Sailor, M. J.; Bhatia, S. N. Computationally Guided Photothermal Tumor Therapy Using Long-Circulating Gold Nanorod Antennas. *Cancer Res.* **2009**, *69*, 3892–3900.
44. Huang, X. H.; Peng, X. H.; Wang, Y. Q.; Wang, Y. X.; Shin, D. M.; El-Sayed, M. A.; Nie, S. M. A Reexamination of Active and Passive Tumor Targeting by Using Rod-Shaped Gold Nanocrystals and Covalently Conjugated Peptide Ligands. *ACS Nano* **2010**, *4*, 5887–5896.
45. Keren, S.; Zavaleta, C.; Cheng, Z.; de la Zerda, A.; Gheysens, O.; Gambhir, S. S. Noninvasive Molecular Imaging of Small Living Subjects Using Raman Spectroscopy. *Proc. Natl. Acad. Sci. U.S.A.* **2008**, *105*, 5844–5849.
46. Mohs, A. M.; Mancini, M. C.; Singhal, S.; Provenzale, J. M.; Leyland-Jones, B.; Wang, M. D.; Nie, S. Hand-Held Spectroscopic Device for *in Vivo* and Intraoperative Tumor Detection: Contrast Enhancement, Detection Sensitivity, and Tissue Penetration. *Anal. Chem.* **2010**, *82*, 9058–9065.
47. Wang, X.; Qian, X. M.; Beitler, J. J.; Chen, Z. G.; Khuri, F. R.; Lewis, M. M.; Shin, H. J. C.; Nie, S. M.; Shin, D. M. Detection of Circulating Tumor Cells in Human Peripheral Blood Using Surface-Enhanced Raman Scattering Nanoparticles. *Cancer Res.* **2011**, *71*, 1526–1532.
48. Huang, X. H.; Neretina, S.; El-Sayed, M. A. Gold Nanorods: From Synthesis and Properties to Biological and Biomedical Applications. *Adv. Mater.* **2009**, *21*, 4880–4910.
49. Vigderman, L.; Khanal, B. P.; Zubarev, E. R. Functional Gold Nanorods: Synthesis, Self-Assembly, and Sensing Applications. *Adv. Mater.* **2012**, *24*, 4811–4841.
50. Hauck, T. S.; Jennings, T. L.; Yatsenko, T.; Kumaradas, J. C.; Chan, W. C. W. Enhancing the Toxicity of Cancer Chemotherapeutics with Gold Nanorod Hyperthermia. *Adv. Mater.* **2008**, *20*, 3832–3838.
51. Ma, X.; Tao, H.; Yang, K.; Feng, L.; Cheng, L.; Shi, X.; Li, Y.; Guo, L.; Liu, Z. A Functionalized Graphene Oxide-Iron Oxide Nanocomposite for Magnetically Targeted Drug Delivery, Photothermal therapy, and Magnetic Resonance Imaging. *Nano Res.* **2012**, *5*, 199–212.
52. Nederberg, F.; Connor, E. F.; Moller, M.; Glauser, T.; Hedrick, J. L. New Paradigms for Organic Catalysts: The First Organocatalytic Living Polymerization. *Angew. Chem., Int. Ed.* **2001**, *40*, 2712–2715.
53. Tsuji, H.; Miyauchi, S. Enzymatic Hydrolysis of poly(Lactide)s: Effects of Molecular Weight, L-Lactide Content, and Enantiomeric and Diastereoisomeric Polymer Blending. *Biomacromolecules* **2001**, *2*, 597–604.
54. Samarajeewa, S.; Shrestha, R.; Li, Y.; Wooley, K. L. Degradability of Poly(Lactic Acid)-Containing Nanoparticles: Enzymatic Access through a Cross-Linked Shell Barrier. *J. Am. Chem. Soc.* **2011**, *134*, 1235–1242.
55. Jain, P. K.; Huang, X. H.; El-Sayed, I. H.; El-Sayed, M. A. Noble Metals on the Nanoscale: Optical and Photothermal Properties and Some Applications in Imaging, Sensing, Biology, and Medicine. *Acc. Chem. Res.* **2008**, *41*, 1578–1586.
56. Murphy, C. J.; Gole, A. M.; Stone, J. W.; Sisco, P. N.; Alkilany, A. M.; Goldsmith, E. C.; Baxter, S. C. Gold Nanoparticles in Biology: Beyond Toxicity to Cellular Imaging. *Acc. Chem. Res.* **2008**, *41*, 1721–1730.
57. Coffey, D. S.; Getzenberg, R. H.; DeWeese, T. L. Hyperthermic Biology and Cancer Therapies a Hypothesis for the "Lance Armstrong Effect". *JAMA, J. Am. Med. Assoc.* **2006**, *296*, 445–448.
58. Yamashita, T.; Ji, J. F.; Budhu, A.; Forgues, M.; Yang, W.; Wang, H. Y.; Jia, H. L.; Ye, Q. H.; Qin, L. X.; Wauthier, E.; *et al.* EpCAM-Positive Hepatocellular Carcinoma Cells Are Tumor-Initiating Cells With Stem/Progenitor Cell Features. *Gastroenterology* **2009**, *136*, 1012–1024.
59. Kimura, O.; Takahashi, T.; Ishii, N.; Inoue, Y.; Ueno, Y.; Kogure, T.; Fukushima, K.; Shiina, M.; Yamagiwa, Y.; Kondo, Y.; *et al.* Characterization of the Epithelial Cell Adhesion

Molecule (EpCAM)$^{+}$ Cell Population in Hepatocellular Carcinoma Cell Lines. *Cancer Sci.* **2010**, *101*, 2145–2155.
60. Hui, K. M. Human Hepatocellular Carcinoma: Expression Profiles-Based Molecular Interpretations and Clinical Applications. *Cancer Lett* **2009**, *286*, 96–102.
61. Anker, J. N.; Hall, W. P.; Lyandres, O.; Shah, N. C.; Zhao, J.; Van Duyne, R. P. Biosensing with Plasmonic Nanosensors. *Nat. Mater.* **2008**, *7*, 442–453.
62. Vasir, J. K.; Labhasetwar, V. Biodegradable Nanoparticles for Cytosolic Delivery of Therapeutics. *Adv. Drug Delivery Rev.* **2007**, *59*, 718–728.
63. Lee, E. S.; Oh, K. T.; Kim, D.; Youn, Y. S.; Bae, Y. H. Tumor pH-Responsive Flower-Like Micelles of Poly(L-Lactic Acid)-*b*-Poly(Ethylene Glycol)-*b*-Poly(L-Histidine). *J. Controlled Release* **2007**, *123*, 19–26.
64. Park, H.; Yang, J.; Lee, J.; Haam, S.; Choi, I. H.; Yoo, K. H. Multifunctional Nanoparticles for Combined Doxorubicin and Photothermal Treatments. *ACS Nano* **2009**, *3*, 2919–2926.
65. Khatua, S.; Manna, P.; Chang, W. S.; Tcherniak, A.; Friedlander, E.; Zubarev, E. R.; Link, S. Plasmonic Nanoparticles−Liquid Crystal Composites. *J. Phys. Chem. C* **2009**, *114*, 7251–7257.
66. Goulet, P. J. G.; Leonardi, A.; Lennox, R. B. Oxidation of Gold Nanoparticles by Au(III) Complexes in Toluene. *J. Phys. Chem. C* **2012**, *116*, 14096–14102.
67. Nikoobakht, B.; El-Sayed, M. A. Preparation and Growth Mechanism of Gold Nanorods (NRs) Using Seed-Mediated Growth Method. *Chem. Mater.* **2003**, *15*, 1957–1962.